npj | urban sustainability

Article

Published in partnership with RMIT University

https://doi.org/10.1038/s42949-025-00277-x

Increasing tree canopy lowers urban air temperature by up to 1.5 °C in heat-prone areas

Masoud Zaerpour[1] ✉, Simon Michael Papalexiou[1,2,3] & Alain Pietroniro[1]

Urban heat islands (UHIs) exacerbate thermal stress, disproportionately affecting communities with limited tree cover. While satellite-derived land surface temperature (*T*s) is widely used to assess urban heat, it often overestimates conditions compared to air temperature (*T*a)—the metric more relevant to human thermal comfort. Despite this discrepancy, relatively few studies have leveraged *T*a to quantify the cooling effect of tree canopy in heat-prone areas. Using a citywide network of high-accuracy air temperature sensors and high-resolution satellite data during a heatwave, we first show that surface UHI (SUHI) overestimates urban heat by a factor of two, with SUHI averaging 8.9 °C ± 1.2 vs 4.6 °C ± 1.1 for canopy UHI. We find that tree canopy cover is the dominant cooling factor, explaining 67% of the spatial variation in *T*a. Notably, a 10% increase in tree canopy reduces air temperature by 0.8 °C, while a 30% increase lowers it by as much as 1.5 °C. These findings underscore the essential role of urban greening in mitigating extreme heat, reinforcing the need for targeted tree-planting strategies in vulnerable neighborhoods. By bridging remote sensing with in-situ temperature observations, our study highlights the urgency of integrating air temperature–based UHI assessments into urban planning and climate adaptation policies. Expanding tree canopy coverage is a scalable, nature-based solution for enhancing urban resilience, and this work directly quantifies its impacts.

Urbanization has transformed local climates, primarily through alterations in land cover and increased anthropogenic heat emissions, which intensify the urban heat island (UHI) effect[1,2]. The UHI effect refers to the phenomenon where urban areas experience higher temperatures than surrounding rural areas due to human activities and modified landscapes. Over the past century, the global urban population has surged—from approximately one-third in 1950 to over half by 2008—with projections indicating that two-thirds of the world's population will reside in urban areas by 2050[3,4]. This rapid urban expansion has amplified the UHI effect, elevating urban temperatures and influencing the health and well-being of residents[5–7]. The situation is further aggravated by climate change[8,9], which intensifies the UHI effect and increases the vulnerability of cities to heat stress[10–12]. Excessive urban heat exacerbates indoor and outdoor thermal discomfort and increases mortality risks, particularly during extreme temperature events[13–16]. High temperatures not only raise the incidence and mortality of urban diseases—with mortality rates rising by 2% for each 1 °C increase in air temperature above 28 °C[17,18]—but also drive a surge in electricity demand for cooling, with air conditioning and refrigeration accounting for a 5–15% increase in energy consumption during heat events[19–21]. These conditions place additional stress on urban infrastructure and energy systems, particularly during peak demand periods[22]. With global temperatures rising at an unprecedented rate due to climate change, understanding and mitigating urban heat impacts has become increasingly urgent[23].

Urbanization has also led to the decline of green spaces, such as trees, and blue spaces, including lakes, rivers, and ponds, which are essential for mitigating urban heat. Green spaces cool urban areas through shading and evapotranspiration, while blue spaces can provide daytime cooling via evaporation and heat buffering. However, due to their high thermal inertia and heat capacity, water bodies may retain heat and contribute to localized warming during the night[24–28]. The integration of green and blue spaces has the potential to enhance urban aerodynamics, increase evapotranspiration, and improve the vertical transport of heat, air, and pollutants, offering a strategy for UHI mitigation[29]. This has prompted growing interest in nature-based solutions, with both urban greening and the restoration or

[1]Department of Civil Engineering, Schulich School of Engineering, University of Calgary, Calgary, Canada. [2] Institute of Global Water Security, Hamburg University of Technology, Hamburg, Germany. [3] Institute for Water, Environment and Health, United Nations University, Hamilton, Canada.
✉e-mail: masoud.zaerpour@ucalgary.ca

incorporation of blue spaces gaining attention as effective strategies to alleviate urban heat[15,30,31].

The cooling efficiency of green spaces, particularly trees, is influenced by climatic conditions, soil moisture, seasonal variations, and their interactions with other urban features[10,30,32–34]. Trees exhibit significant cooling effects during warm periods, with greater temperature reductions in summer than in winter[35–37]. However, under conditions such as heatwaves or limited soil moisture, their cooling potential may diminish due to reduced transpiration rates[30,38]. Importantly, the cooling efficiency of tree canopies is also scale-dependent, varying with spatial context and their interactions with other factors, such as the type and extent of impervious surfaces[26]. These interactions can either enhance or suppress the cooling effect of trees, complicating efforts to disentangle their contribution to UHI from other impactful variables. While the benefits of trees have been extensively studied during peak summer heat, the interplay between tree canopy, climate, soil moisture, and urban morphology across diverse climatic contexts remains less understood.

Similarly, blue spaces, such as lakes and ponds, mitigate daytime UHI by leveraging their high heat capacity and evaporative cooling properties[39–41]. Water bodies create a localized urban cool island effect by reducing air and surface temperatures through their high heat capacity, which allows them to warm more slowly than surrounding materials, and through evaporation and convection processes[41–43]. Studies have shown that these features can reduce urban temperatures by up to 6 °C, providing immediate thermal relief[30,39,44–46]. However, due to their high thermal inertia, large water bodies may retain heat and potentially contribute to localized nighttime warming, particularly in warmer climates or areas with limited nighttime ventilation[27,28,47]. Enhancing the integration of green and blue spaces in urban areas offers a promising avenue for achieving sustainable cooling strategies. Yet, much of the research on blue spaces has focused on isolated features, leaving their collective impacts underexplored[48].

Most studies assessing the cooling effect of water bodies and trees have relied on land surface temperature (Ts) from remote sensing due to its high spatial resolution and widespread availability[17,18,30,49–51]. However, Ts primarily reflects surface heat island effect (SUHI) and may not accurately capture canopy UHI (CUHI) measured by ambient air temperature (Ta), which is more relevant to human thermal comfort[36,48,52,53]. Ta, measured by in-situ sensors, provides a direct reflection of human-perceived temperatures, but its spatial coverage is often limited due to the high cost of sensor networks[52,54]. In recent years, crowdsourced temperatures have emerged as an alternative, but issues related to sensor placement, solar exposure, and data inconsistencies undermine their reliability[52,55–57].

To address these challenges, this study combines high-quality Ta data from a city-managed sensor network with satellite-derived Ts observations, focusing on Ts–Ta relationship and bridging the gap between surface and ambient urban heat assessments[32]. This relationship, however, is complex, influenced by the distinct radiative and conductive properties of surfaces and air, which respond differently to solar heating and heat storage[48,53,58,59]. Unlike studies that rely on crowdsourced or opportunistic air temperature measurements, which may suffer from inconsistent sensor placement and calibration[52,56], our approach utilizes a dedicated sensor network designed for high accuracy and reliability[60]. These well-maintained sensors ensure standardized data collection, reducing uncertainties and improving the robustness of urban temperature assessments. By spatiotemporally matching satellite-derived Ts with ground-based air temperature (Ta) observations at sensor locations, we develop a machine learning model that estimates the anomaly between Ta and Ts (i.e., Ts–Ta) across urban areas. The model uses various urban and climatic predictors to quantify Ts–Ta relationship, enabling a more nuanced understanding of UHI dynamics.

We apply this approach to Calgary, Alberta—a mid-sized Canadian city with strong seasonal temperature contrasts, rich spatial data, and a dense ground-based sensor network. Calgary also offers a timely case for urban heat research, having experienced several extreme heat events in recent years, including a record-setting heatwave in 2021. These characteristics make Calgary well-suited to explore intra-urban temperature variability and evaluate the effectiveness of urban greening as a mitigation strategy. Moreover, the findings from this study are broadly applicable to other mid-latitude cities experiencing similar climatic and development pressures.

The approach is a dual-model framework that consists of two components: the vertical thermal gradient (V-TG) model and the horizontal urban heat island (H-UHI) model. First, the V-TG model uses machine learning techniques, specifically XGBoost, to estimate the relationship between surface temperature (Ts) and ambient air temperature (Ta), incorporating key urban and climatic features. This model generates high-resolution temperature anomaly estimates that reveal the spatial patterns of UHI across the city. Building on these estimates, the H-UHI model explains spatial drivers of UHI intensity by integrating factors such as building density (BD), tree canopy ratio, and climatic influences. The study leverages a comprehensive dataset from a city-installed sensor network, integrating lidar-measured tree canopy data with satellite observations. This approach enables a deeper understanding of the cooling contributions of tree canopies, which are influenced by their interactions with urban morphology, climatic conditions, and impervious surfaces. In contrast to previous studies that focus on either Ts–Ta comparisons or coarse-scale UHI modeling, this study introduces a two-stage machine learning framework that combines detailed observational data with scenario-based analysis of greening interventions. By disentangling the effects of these factors, the study presents a way to assess the compound impact of green spaces in mitigating UHI. This framework highlights the distinct and synergistic roles of tree canopy cover in reducing urban temperatures and informs spatially optimized urban design strategies to enhance resilience to climate change and improve thermal comfort in cities globally.

Results

The V-TG model was trained using sensor-derived air temperature (Ta) measurements from 21 ground-based sensors deployed across central Calgary (see Supplementary Fig. 1). These sensors captured minute-scale temperature variations from 2021 to 2024, ensuring a comprehensive representation of urban heat dynamics. Additionally, Landsat 8 and 9 satellite-derived surface temperature (Ts) data were used to model the relationship between air and surface temperatures. For a detailed explanation of the data sources, preprocessing steps, and modeling approach, please refer to the "Methods" section. The model incorporates a set of relevant urban and climatic features used for training, including tree canopy ratio (TC), BD, building height (BH), floor area ratio (FAR), sky view factor (SVF), shadow height (SH), impervious/pervious surface ratios (SR), relative humidity (H), wind speed (WS), and WD—see Supplementary Table 1. To assess the influence of spatial scale, we extracted these features within circular buffers of varying radii (50 m, 70 m, 100 m, 150 m, and 200 m) around each sensor and trained the model across different buffer distances. These features help quantify the complex interactions between urban morphology, vegetation, and climate by capturing their effects on shading, evapotranspiration, heat retention, and airflow—key processes that drive temperature anomalies.

To assess the model's reliability and predictive capability, we first evaluate its performance in estimating anomalies between Ta and Ts, as shown in Fig. 1. The figure presents the mean root mean square error (RMSE), coefficient of determination (R^2) values, and mean absolute error MAE across different buffer distances (50 m, 70 m, 100 m, 150 m, and 200 m) surrounding 21 monitoring stations in the center of the city. The model's performance varies with buffer distance, demonstrating the strongest predictive accuracy at a radius of 50 m. At this scale, the model achieves the lowest mean RMSE of 1.78 °C and a high R^2 value of 0.86, indicating strong agreement between predicted and observed temperature anomalies. The MAE at this radius is also minimal at 1.30 °C, reflecting the model's best accuracy at a radius of 50 m. Additionally, the mean error (ME) is 0.01 °C, and the standard deviation of errors is lowest at the 50-m radius, indicating reduced uncertainty in

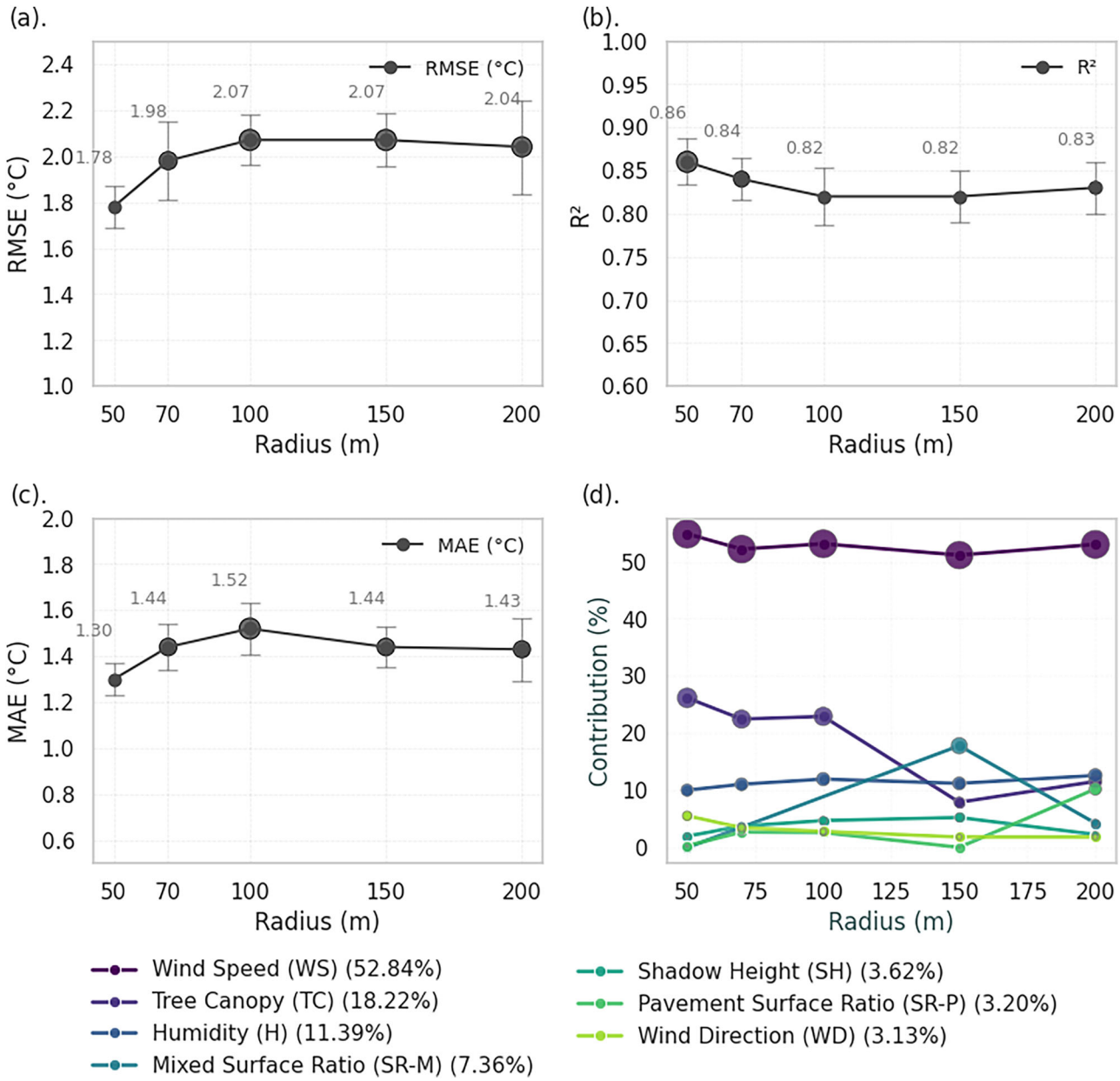

Fig. 1 | Performance metrics and key feature contributions of the V-TG model in predicting temperature anomalies. Performance metrics of the V-TG model in predicting anomalies between sensor-derived air temperature (*T*a) and Landsat surface temperature (*T*s) across varying buffer distances. **a**–**c** Display the mean RMSE, R^2, and MAE, respectively, for buffer radii of 50 m, 70 m, 100 m, 150 m, and 200 m. Error bars indicate the standard deviation of the metrics derived from five cross-validation runs. Additionally, **d** presents feature contributions at different radii, with only features contributing more than 1% on average to the model predictions being displayed. WS, tree canopy ratio (TC), and relative humidity (H) are identified as the most influential factors. The improved model accuracy at a 50-m radius is emphasized, which exhibited the lowest RMSE and highest R^2 values.

model performance across the five cross-validation runs. Although the RMSE values may appear high in absolute terms, they are reasonable relative to the wide range of *T*s–*T*a anomalies observed across the study area (Supplementary Fig. 2).

To better understand the factors influencing temperature anomalies, we analyzed the contributions of individual features using SHAP values. SHAP is an approach that assigns each feature an importance value for a particular prediction, helping to interpret complex machine learning models by quantifying how much each feature contributes to the model's output. Among the key contributors, WS accounted for the largest share of variance at 54.84%, followed by tree canopy ratio (TC) at 26.7% and relative humidity (H) at 10.59% at the 50-m radius. While the effect of WS remains relatively stable across increasing buffer distances, the influence of TC declines significantly, dropping from 26.7% at 50 m to less than 8% beyond 100 m. This suggests that the impact of tree canopy is more localized, whereas broader-scale influences such as WS remain more consistent. Other urban features, including FAR, BD, SVF, and SH, also contribute to temperature anomalies, underscoring the multifaceted nature of urban heat dynamics.

We then estimated *T*a for 36,123 spatially distributed 50 × 50 m grids covering the central region of the city using the V-TG model. The performance of the H-UHI model is evaluated in explaining urban heat intensity across the city. This model quantifies temperature differences between the estimated air temperature (*T*a) at each grid point and a reference station located outside the urban core, allowing for a spatially explicit assessment of canopy urban heat island (CUHI) effects. The performance of the H-UHI

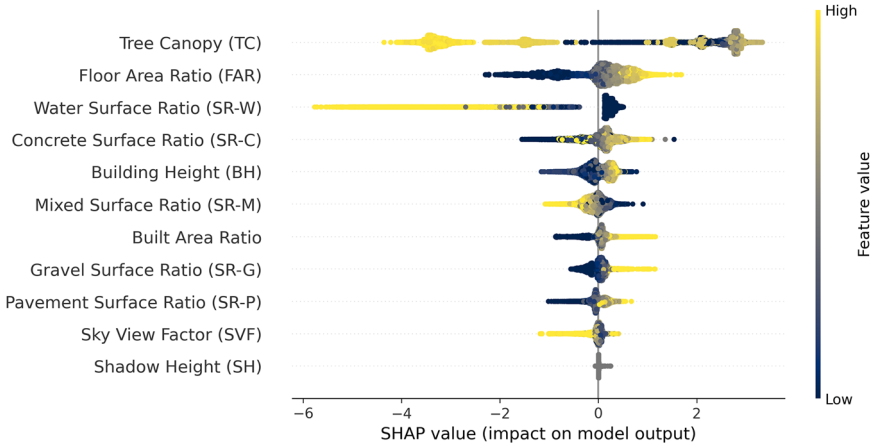

Fig. 2 | SHAP summary plot of feature contributions to H-UHI estimations. SHAP summary plot illustrating feature contributions to temperature differences as predicted by the H-UHI model. The plot showcases the relative importance of various features, with contributions represented as a SHAP value. Features are ranked from top to bottom based on their relative importance, with those having the highest contributions appearing at the top of the chart. A higher SHAP value indicates a greater impact on temperature differences between grid points and the reference station.

model was assessed through five-fold cross-validation, yielding an RMSE of 1.53 °C, a mean R^2 of 0.82, a MAE of 1.13 °C, and an ME of 0.02 °C.

To better understand the factors driving these temperature variations, we analyzed feature contributions using SHAP values (Fig. 2). Among the contributors, the tree canopy ratio (TC) emerged as the most dominant factor, accounting for approximately 57% of the temperature variation. Other influential features included FAR, contributing 11.66%, and the water surface ratio (SR-W), at 9.35%. These percentages were calculated by summing the absolute SHAP values for each feature across all observations and dividing by the total sum of absolute SHAP values for all features. This provides a normalized measure of relative importance across predictors.

As previously discussed, tree canopy coverage plays a crucial role in regulating urban temperatures. To quantify its potential impact under extreme heat conditions, we conducted a hotspot analysis and scenario-based assessment using estimated air temperatures for a representative day during the July 2023 heatwave, when portions of the city exceeded the official heatwave threshold of 29 °C as defined for Calgary by Environment and Climate Change Canada (ECCC)[61]. Increasing canopy cover can mitigate rising temperatures in urban hotspots. On this day, hotspots—defined as areas where *T*a exceeded 29 °C—were identified across 13,306 urban grids. To explore the potential cooling effect of enhanced tree cover, we simulated three scenarios with incremental increases of 10%, 20%, and 30% in canopy coverage across these hotspots. These hotspots were spatially distributed throughout the city. In each scenario, the existing tree canopy area for these grids was increased by the specified percentage, and the resulting changes in *T*a were estimated using the calibrated H-UHI model.

The results indicate a progressive reduction in hotspot temperatures (Fig. 3). Under Scenario 1 (S1: 10% increase), 11.6% of hotspot grids dropped below 29 °C, which increased to 18.0% in Scenario 2 (S2: 20% increase) and further to 31.6% in Scenario 3 (S3: 30% increase). Correspondingly, the mean *T*a values decreased from the current 31 °C ± 1.01 to 30 °C ± 0.89 under S1, 29.6 °C ± 0.97 under S2, and 29.2 °C ± 1.0 under S3. While we did not explicitly quantify the functional form of this relationship, these results suggest that the cooling effect of increasing tree canopy coverage is not strictly linear, as equal percentage increases in canopy area do not yield equal temperature reductions. Importantly, the effectiveness of tree canopy is also influenced by additional factors, such as impervious surface types and built-up density (FAR), which affect the extent of temperature reduction and contribute to the observed effect.

Building on this analysis, we extended our investigation to assess tree canopy distribution and urban heat exposure across the entire City of Calgary. Specifically, we examined the relationships between median household income, surface temperature (*T*s), and tree canopy coverage across 290 neighborhoods. This broader perspective, illustrated in Fig. 4, reveals significant disparities in heat exposure and tree equity. In particular, economically vulnerable neighborhoods in the eastern part of the city experience disproportionately higher temperatures during heatwaves, largely due to

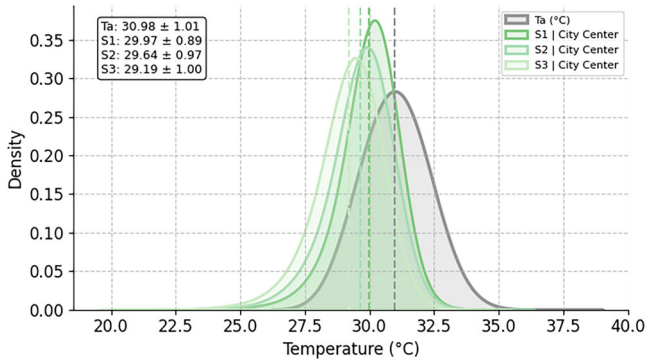

Fig. 3 | Impact of enhanced tree canopy coverage on air temperature distribution in urban hotspots. Distribution of air temperature *T*a across urban hotspots in the city's central area under current conditions and three scenarios of increased tree canopy coverage (10%, 20%, and 30%). The distribution illustrates the variation in *T*a, with dashed lines representing the mean temperatures for each scenario. The results indicate a progressive reduction in temperature with increased tree canopy coverage.

lower tree canopy coverage. Further analysis demonstrates a clear association between lower median household incomes and increased air temperatures during heatwaves (Spearman correlation = −0.56; see Supplementary Fig. 3).

Statistical analysis further supports this observation, revealing a significant negative correlation (Spearman correlation = −0.49) between tree canopy coverage and *T*s (see Supplementary Fig. 4). Areas with lower tree canopy coverage consistently endure higher temperatures, reinforcing the role of vegetation in moderating urban heat exposure.

To further quantify urban heat intensity, we estimated *T*a across all 330,073 grids citywide and compared the estimated temperature differences with a reference station outside the city core, which recorded 26.6 °C around 12:30 PM on a day during the July 2023 heatwave. The results, shown in Fig. 5a, highlight a significant discrepancy between satellite-based and sensor-based UHI estimations. The satellite-derived surface urban heat island (SUHI), measured by *T*s differences (mean: 8.9 °C ± 1.2), overestimates urban heat intensity by nearly twofold compared to sensor-derived CUHI, measured by *T*a differences (mean: 4.6 °C ± 1.1).

To explore potential mitigation strategies, we simulated the impact of increased tree canopy coverage (10%, 20%, and 30%) across the city's 36,582 hotspot grids. The results (Fig. 5b) demonstrate a progressive reduction in average hotspot temperatures, with decreases of 0.8 °C, 1.1 °C, and 1.5 °C, respectively.

Discussion

The use of sensor-based data in this study offers significant advantages over crowdsourced or satellite-derived LST data, providing a reliable estimate of

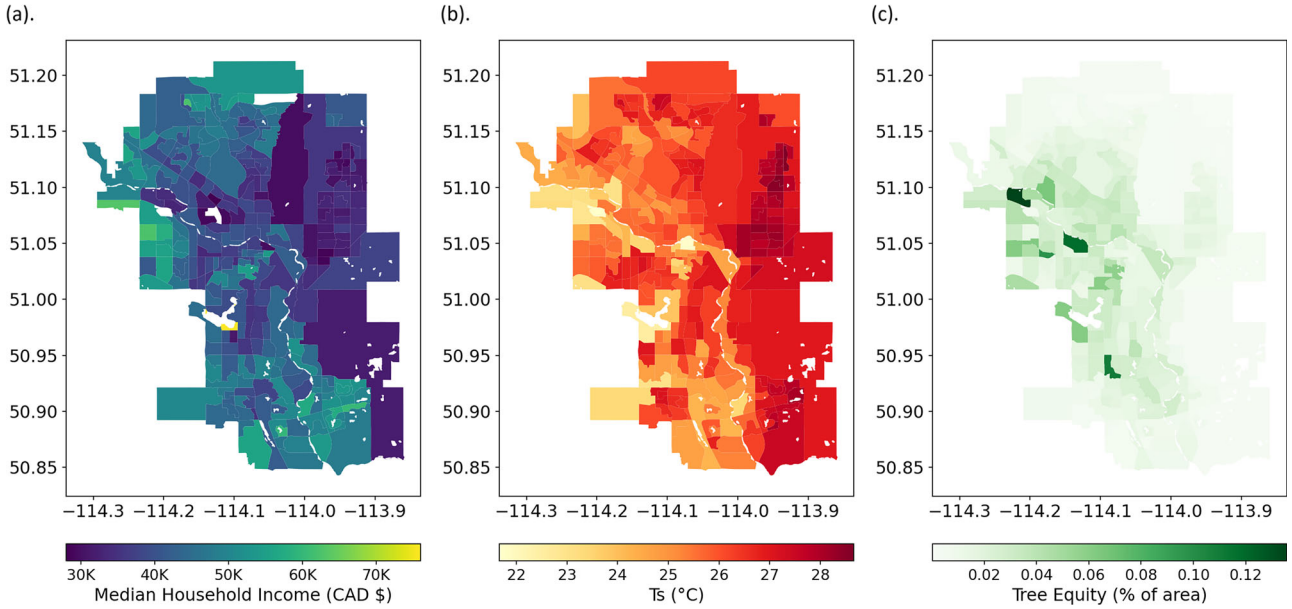

Fig. 4 | Spatial inequities in income, surface temperature, and tree canopy coverage across neighborhoods. Spatial distribution of aggregated variables across 290 neighborhoods in the study area: **a** median household income (in thousands of CAD), **b** average *T*s (°C), and **c** tree equity (percentage of area covered by trees). The figure highlights that economically vulnerable neighborhoods in the eastern part of the city experience higher temperatures and have less tree canopy cover compared to other areas.

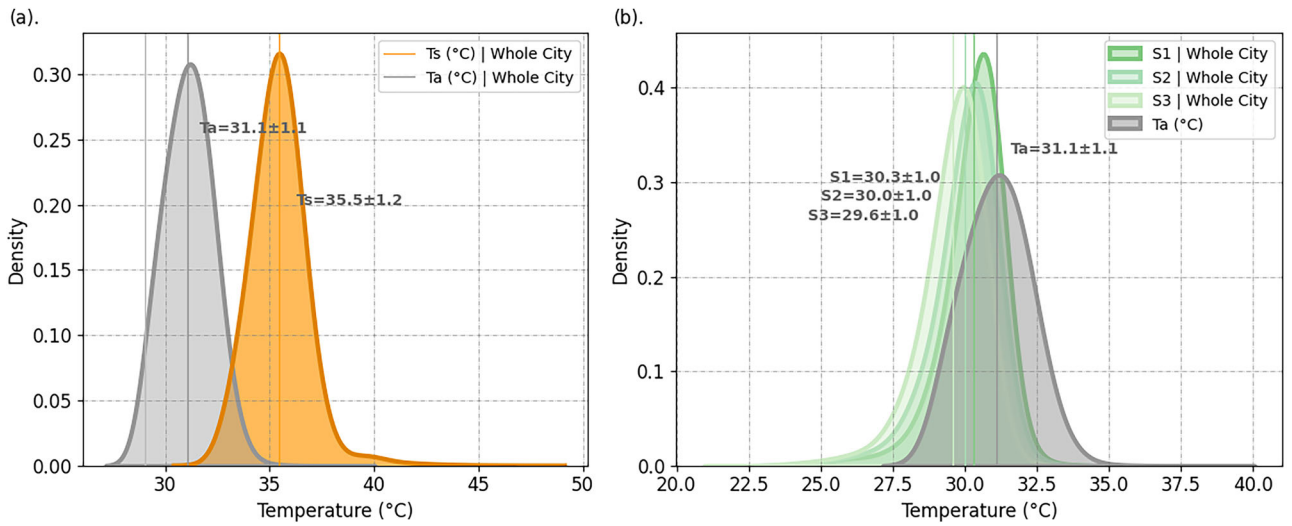

Fig. 5 | Probability distributions and the impact of tree canopy scenarios on urban heat mitigation. a Probability distribution of satellite-measured surface temperatures (*T*s, in orange) and sensor-derived air temperatures (*T*a, in gray) across all analyzed grids. The average SUHI intensity, measured by *T*s (mean: 8.9 °C ± 1.2), is approximately twice as high as the average CUHI intensity, measured by *T*a (mean: 4.6 °C ± 1.1), when compared to a reference station outside the city (*T* = 26.6 °C during the 2023 heatwave). **b** Probability distributions of *T*a and simulated hotspot temperatures under three tree canopy enhancement scenarios (S1: 10%, S2: 20%, and S3: 30% increase). Progressive increases in tree canopy coverage lead to consistent reductions in average hotspot temperatures (S1: −0.8 °C, S2: −1.1 °C, S3: −1.5 °C), showcasing the significant cooling potential of urban greening strategies.

localized UHI dynamics. Crowdsourced data, while valuable[52,62], often suffers from biases and inconsistencies[52], whereas sensors deliver uniform and reliable measurements[32]. These methodological improvements allow for a more accurate assessment of urban features and mitigation strategies, addressing the limitations of satellite-derived LST. This underscores the value of sensor networks in urban climate research.

Our analysis of the *T*s–*T*a relationship revealed that factors such as WS, tree canopy ratio, and relative humidity exerted the most significant influence on temperature anomalies, collectively explaining around 90% of the variance within a 50-m radius. WS emerged as the dominant factor, accounting for 54.84% of the contributions, due to its ability to disperse heat and reduce localized warming[63,64]. Tree canopy ratio, contributing 26.7%, mitigates surface heating through shading and evapotranspiration, while relative humidity, with a 10.59% contribution, modulates the thermal gradient by affecting evaporative cooling processes. This is especially crucial, as more recent assessments have emphasized the complex and climate-dependent interplay between tree canopy, relative humidity, and urban airflow dynamics in shaping air temperature variations[65–67]. By explicitly considering these interactions, our analysis provides a more comprehensive understanding of the cooling impact of tree canopy on air temperature, demonstrating how its effects are modulated by atmospheric conditions such as WS and relative humidity. This nuanced perspective highlights the

importance of integrating multiple environmental factors rather than analyzing tree canopy effects alone.

While these key variables played a dominant role in shaping temperature anomalies, other factors such as SVF and SH had a more limited influence on the *T*s–*T*a relationship. This is primarily because the Landsat-derived surface temperature measurements were captured around noon, when solar zenith angles are high and shadows are minimal[68]. As a result, the effects of urban morphology on shading and radiative cooling, which tend to be more pronounced during morning or late afternoon, were not fully captured. This finding contrasts with studies from regions like Hong Kong, where dense urban canyons and prolonged shadow durations influence thermal dynamics throughout the day[69–71]. These results highlight the critical role of measurement timing in interpreting the interplay between urban structure and thermal gradients, emphasizing the need to incorporate diurnal variations and temporal dynamics in future UHI assessments. In particular, our framework does not capture nighttime UHI intensity—often more pronounced in dense urban areas due to delayed heat release—because Landsat provides only daytime observations. While other satellite products can offer nighttime surface temperature data, they typically operate at much coarser spatial resolutions, making them less suitable for high-resolution urban analyses.

SUHI, derived from land surface temperature (*T*s), has been extensively used in the literature to study UHI effects due to its wide spatial coverage and ease of access through satellite imagery[52,72]. However, our findings suggest that *T*s tends to overestimate UHI intensity relative to air temperature *T*a-based measurements. Specifically, we found that city-scale UHI intensity was overestimated by a factor of two when *T*s was used instead of *T*a. This discrepancy arises from the distinct physical processes governing *T*s and *T*a. Surface temperature responds rapidly to incoming solar radiation and is influenced by material-specific properties such as albedo, emissivity, and moisture content. In contrast, air temperature is shaped not only by radiative exchange but also by convective and advective processes, as well as anthropogenic heat emissions and thermal inertia of the built environment[48]. As a result, surface heating tends to be more intense and localized compared to the more buffered response of ambient air. Importantly, this comparison was made using matched daytime observations collected around 12:30 PM local time, coinciding with the Landsat overpass, to ensure temporal consistency between SUHI and CUHI estimates. While SUHI and CUHI can differ in both sign and magnitude depending on time of day[73], our focus on daytime conditions aligns with prior studies[52] which also demonstrated SUHI overestimation using satellite data. This reinforces the importance of integrating both surface and atmospheric thermal metrics to produce more accurate and human-relevant assessments of urban heat exposure.

Focusing on the H-UHI model and the relative contributions of features, our analysis effectively disentangles the effects of tree canopy and water bodies on UHI mitigation by leveraging sensor data and controlling for confounding factors such as urban morphology, land cover, and climatic variables. By isolating these effects, we found that tree canopy exerts a stronger cooling influence on UHI than other factors, explaining 57% of variations in *T*a. It aligns with previous research, emphasizing the critical role of trees/green spaces in reducing urban heat through evapotranspiration and shading[17,18,42,53,74]. Built-up areas (FAR) also emerged as a driver of UHI intensity, accounting for 11.6% of spatial variations in *T*a, reflecting the influence of BD and heat retention, which confirms previous studies[32,75,76]. Additionally, our results highlight the scale-dependent nature of feature contributions[26,52,77], where localized effects, such as tree canopy cooling, are most pronounced at smaller buffer radii (e.g., 50 m) but diminish significantly at larger scales. Specifically, the contribution of tree canopy drops from 26.7% at 50 m to less than 8% beyond 100 m, whereas WS remains a dominant factor across scales. This underscores the importance of considering spatial scale when designing UHI mitigation strategies, as certain factors may be more influential at localized vs broader spatial extents[26,78].

The importance of tree canopy coverage is particularly pronounced for vulnerable, low-income communities that disproportionately experience higher UHI intensities due to limited green space[79]. While much research has focused on variations in UHI intensity across different cities, the disproportionate variation within a single city often goes overlooked[80]. These intra-city differences can significantly affect demographic groups, as certain areas may experience much higher UHI intensities than others. Our findings demonstrate that areas with lower tree canopy consistently experienced higher temperatures, emphasizing the urgent need for greening interventions in underserved neighborhoods[80,81].

The strong impact of tree canopy underscores its role in mitigating UHI effects, with cooling benefits potentially reaching up to 8.2 °C in the best-case scenario for a 30% increase in tree canopy coverage within hotspot areas. On average, a 30% increase in tree canopy coverage results in a temperature reduction of 1.5 °C. Our findings are consistent with previous research, which demonstrated significant temperature reductions due to tree canopy effects[18,34,49,53,72]. We showed that spatially optimized increases in tree canopy (a 10% increase in identified hotspots) can reduce the average temperature by 0.8 °C.

Such initiatives not only reduce heat exposure but also alleviate health disparities and enhance thermal comfort for low-income populations during extreme heat events. By prioritizing targeted greening interventions in underserved neighborhoods, cities can address heat disparities, improve public health outcomes during extreme heat events, and foster equitable urban environments. However, during acute heatwave events, greening efforts must be complemented by city-wide heat action plans. These can include establishing public cooling centers, issuing early heat warnings, and increasing community outreach to protect vulnerable populations. In addition, strategies that enhance natural ventilation—such as maintaining open spaces, preserving wind corridors, and reducing building-induced airflow blockages—can help amplify the cooling effect of greening and improve thermal comfort in the short term.

This study highlights the critical role of sensor-derived air temperature (*T*a) data in accurately assessing UHI effects, emphasizing the importance of localized and reliable measurements over satellite-derived surface temperatures (*T*s). The V-TG model demonstrated high accuracy in predicting *T*a anomalies, with the 50-m buffer radius yielding optimal performance metrics (RMSE = 1.78 °C, $R^2 = 0.86$). Although the RMSE may appear relatively large at first, it is moderate when contextualized against the wide range of observed *T*s-*T*a anomalies across the study area (−5 °C to +16 °C, with a median of 3.64 °C). While this performance is robust relative to the wide range of observed *T*s-*T*a anomalies, residual model errors may still propagate into the model estimates and should be considered when interpreting UHI magnitudes. Nevertheless, because the model is unbiased on average (ME = 0.01 °C), spatially aggregated UHI estimates—such as the average *T*a difference across thousands of urban grids—remain reliable. The results further reveal that WS, tree canopy ratio, and relative humidity are the most influential factors, collectively accounting for approximately 90% of the variance in *T*s-*T*a anomalies. These findings underline the significance of fine-scale spatial features in shaping urban temperature dynamics.

The H-UHI model provided robust insights into UHI patterns across the city, further showcasing the critical cooling role of tree canopy, which explained 57% of *T*a variations. Scenario-based analyses of increased canopy coverage demonstrated the potential to mitigate extreme urban heat, particularly in hotspots. A 30% increase in tree canopy coverage reduced mean hotspot temperatures by 1.5 °C and significantly decreased the number of grids exceeding 29 °C. The results highlight the nonlinear cooling effect of tree canopy enhancements and the substantial benefits of urban greening initiatives.

Balanced urban planning is essential to integrate compact urbanization with adequate green spaces, creating room for tree growth in dense areas without exacerbating urban sprawl[82–84]. Expanding tree canopy coverage is not only a critical strategy for mitigating urban heat but also an opportunity to address disparities in heat exposure and promote social equity. Enhancing

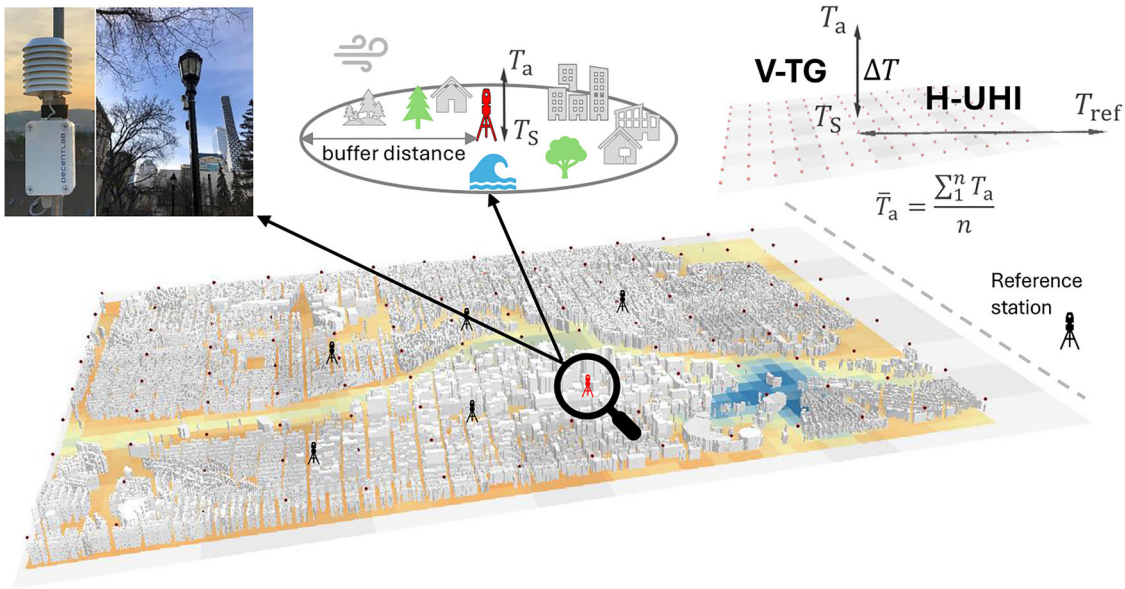

Fig. 6 | Schematic representation of the methodology used to model the temperature anomaly (*Ts–Ta*). The framework integrates climatic variables (e.g., WS, WD, and relative humidity), urban morphology (e.g., BD, BH, FAR, and SVF), and land cover characteristics (e.g., tree canopy ratio and impervious surface ratio) to estimate surface and ambient air temperature differences. The V-TG model first establishes the *T*s–*T*a relationship, which is then applied in the H-UHI model to assess the spatial distribution of the UHI effect. This schematic highlights the key components influencing urban temperature variations. All elements of this schematic were created by the first author using open-source QGIS tools.

tree equity, particularly in lower-income neighborhoods, will strengthen urban resilience to climate change and foster more livable cities, especially during heatwave events.

Our analysis revealed pronounced disparities in heat exposure and tree equity, with lower-income neighborhoods experiencing higher temperatures and reduced vegetation coverage. This spatial inequity, coupled with the overestimation of UHI intensity by *T*s compared to *T*a, highlights the need for targeted interventions to address both environmental and social inequalities. Incorporating *T*a-based measurements provides a more accurate depiction of urban heat intensity, essential for developing equitable climate adaptation strategies.

In conclusion, increasing tree canopy coverage offers a natural and effective solution for mitigating urban heat, enhancing social equity, and improving urban resilience to climate change. Future urban planning efforts must prioritize greening initiatives, particularly in vulnerable neighborhoods, to reduce heat exposure disparities and foster sustainable, climate-adaptive cities. Integrating sensor-based data with traditional satellite observations will further refine our understanding of UHI dynamics and guide the development of actionable policies for urban climate adaptation.

Methods

This study employs two models, the V-TG model and the H-UHI model, to estimate temperature anomalies (*T*s-*T*a) and assess the UHI effect in Calgary. These models integrate various urban and climatic features to better understand the spatial and temporal patterns of UHI across the city, which are detailed below. These models integrate various urban and climatic features to better understand the spatial and temporal patterns of UHI across the city, which are detailed below. Figure 6 provides a schematic overview of the methodology.

Extreme gradient boosting (XGBoost) model

Both the V-TG model and the H-UHI model employed XGBoost, a robust machine learning algorithm renowned for its predictive performance and flexibility. XGBoost has gained widespread recognition for its ability to solve both regression and classification problems effectively[85–87]. XGBoost is a part of the boosting-based techniques family and operates by iteratively improving the prediction accuracy of gradient-boosted decision trees (GBDT). It achieves this by sequentially adding residuals from previous iterations to the tree model, progressively refining predictions while addressing common challenges such as overfitting and computational inefficiency[88]. The *xgboost* package[89] in Python, was employed for the model implementation in this study.

Since the accuracy of machine learning models is highly dependent on their hyperparameter configuration[90–92], optimizing these parameters was a key step in developing both the V-TG and H-UHI models. Proper hyperparameter tuning ensures that the model effectively captures underlying patterns in the data while avoiding issues such as overfitting or underfitting. By refining these parameters, the models achieve a balance between complexity and generalization, ultimately leading to more accurate and reliable predictions.

V-TG model

The V-TG model is used to estimate the relationship between ambient air temperature (*T*a) and surface temperature (*T*s), focusing on the difference between sensor-derived *T*a and Landsat-derived *T*s. *T*s serves as the spatial reference baseline (not a predictor variable), and the model is trained to estimate the difference between sensor-derived *T*a and corresponding Landsat-derived *T*s. To enable this, we matched each *T*s from cloud-free Landsat 8 or 9 scenes (between 2021 and 2024) to the nearest-in-time *T*a measurement from the 21 ground-based sensors. All satellite scenes were acquired around 12:30 PM local time (±15 min), corresponding to the Landsat overpass time over Calgary, ensuring temporal alignment between *T*s and *T*a. The high temporal resolution of the *T*a sensors (minute-scale) allowed for precise temporal alignment with the Landsat overpass times. Once trained, the model estimates the anomaly (*T*a–*T*s), which is then added to the *T*s to estimate air temperature. As the model is trained on daytime *T*a–*T*s anomalies derived from Landsat overpass, it is limited to simulating daytime temperature dynamics and does not account for nighttime UHI effects.

The model integrates various urban and climatic features that influence the temperature anomaly, including urban structure variables (such as BD, BH, and FAR), tree canopy ratio, impervious/pervious surface types, and climatic factors (such as WS, WD, and relative humidity), as illustrated in Fig. 6. These include urban structure variables (such as BD, BH, and FAR),

tree canopy ratio, impervious/pervious surface types, and climatic factors (such as WS, WD, and relative humidity). They are explained in the "Data" section in detail.

To optimize the performance of the V-TG model, a hyperparameter tuning process was conducted using a Random Search approach via *RandomizedSearchCV*[92]. The tuning process focused on key parameters, including the number of boosting iterations (50–500), the learning rate (0.01–0.2), and the maximum depth of decision trees (3–8), ensuring an optimal balance between model complexity and predictive accuracy. The best-performing V-TG model was configured with 300 boosting iterations, a learning rate of 0.01, and a maximum tree depth of 4. RandomizedSearchCV was selected for its computational efficiency and ability to explore a wide range of hyperparameter combinations without requiring an exhaustive search, making it especially suitable for complex models like XGBoost. The parameter ranges were selected to allow the model to flexibly capture complex patterns while minimizing the risk of overfitting. In addition to selecting the best model configuration based on cross-validated performance, we used the squared error loss function as the training criterion in XGBoost models, as this loss function penalizes large prediction errors more heavily, aligning with the study's goal of minimizing deviations in temperature estimation.

To evaluate the generalization capability of the V-TG model, we employed a five-fold cross-validation approach. The dataset was randomly divided into five equally sized folds. In each iteration, the model was trained on four folds (80% of the data) and validated on the remaining fold (20%). This process was repeated five times so that each fold served once as a validation set. The performance metrics (RMSE, R^2, MAE, and ME) reported in the "Results" section represent the mean values across all five iterations.

H-UHI model

Following the estimation of the Ts–Ta relationship in the V-TG model, the H-UHI model is used to evaluate the UHI effect across the city. The H-UHI model utilizes Ta data, estimated through the V-TG model trained with sensor network data. These predictions are applied at different spatial scales, offering a detailed and spatially explicit assessment of UHI intensity across urban areas. Importantly, the H-UHI model functions as an explanatory model that identifies the drivers of spatial differences between air temperature at urban grids and a reference suburban location outside the urban core. The H-UHI model integrates similar urban features, including BD, tree canopy ratio, SVF, and impervious/pervious SR to quantify urban temperature variations and evaluate the UHI effect, as summarized in Fig. 6.

To quantify UHI intensity, we calculated the temperature difference between each grid-level Ta estimate and a suburban reference station. The reference station was selected from the three CRAZ (Calgary region airshed zone) weather stations that record temperature data at a minute scale. Among them, we selected the Inglewood station, located farthest from the built-up downtown core, with low impervious surface coverage and high tree canopy. This location consistently lies outside the core UHI zone, making it a suitable baseline for comparative UHI assessment.

While the temperature differences between the grid Ta estimates and a suburban reference station provide a direct measure of UHI intensity, the H-UHI model is not used to re-estimate this value. Instead, it explains the spatial variability in UHI intensity by modeling how urban morphological and environmental features influence the estimated temperature differences. This explanatory modeling allows us to identify the key factors—such as tree canopy ratio, urban morphology, and impervious surfaces—that shape localized heat exposure across the city. In this way, the H-UHI model complements the V-TG model by revealing the primary drivers of intra-urban heat variation.

The same hyperparameter tuning approach as in the V-TG model was used to determine the optimal configuration for the H-UHI model. The parameter search explored the same ranges, with the number of boosting iterations set between 50 and 500, the learning rate between 0.01 and 0.2, and the maximum tree depth between 3 and 8. The best-performing H-UHI model was obtained with 300 boosting iterations, a learning rate of 0.03, and a maximum tree depth of 5, ensuring reliable spatial predictions of urban air temperature variations. Like the V-TG model, the H-UHI model was trained using the squared error loss function.

The H-UHI model was also validated using a five-fold cross-validation procedure identical to that used for the V-TG model. This allowed us to assess how well the model captures spatial variation in urban air temperature differences relative to a reference station while avoiding overfitting. Each fold used 80% of the data for training and 20% for testing, with average metrics reported across folds to ensure reliability and generalization to unseen grids.

Shapley additive explanations (SHAP)

To increase the interpretability of the XGBoost models, SHAP was applied. We used the TreeExplainer implementation of SHAP, which is specifically designed for tree-based ensemble models such as XGBoost and allows for efficient, consistent calculation of feature attributions. SHAP is a widely used method in explainable artificial intelligence (XAI) that allocates SHAP values to independent variables. This helps in understanding the contribution of each feature to the model's predictions by evaluating their marginal effects[93,94]. By calculating the difference in model predictions when a feature is included vs when it is excluded, SHAP values offer valuable insights into the role of each urban and climatic feature in shaping the predicted temperature anomalies and UHI effect.

The SHAP value ϕ_i for each feature i in n features is:

$$\phi_i = \sum_{S \in F\{i\}} \frac{|S|!(|F| - |S| - 1)!}{|F|!} \left[f_{S\bigcup\{i\}}\left(x_{S\bigcup\{i\}}\right) - f_S(x_S) \right] \quad (1)$$

where F is the set of all combinable features in S, and the difference between the contributions when feature i is employed and when it is not is calculated by $f_{S\bigcup\{i\}}\left(x_{S\bigcup\{i\}}\right) - f_S(x_S)$.

Both the V-TG and H-UHI models integrate a range of urban and climatic features, such as BD, BH, FAR, SVF, and tree canopy ratio. These features, along with climate variables like relative humidity, WS, and WD, contribute to a comprehensive understanding of the spatial distribution of temperature anomalies and the UHI effect. The combination of these factors allows for a detailed analysis of their gradient and marginal effects on the LST-SDA temperature anomaly, thereby providing valuable insights for urban adaptation and mitigation strategies in the face of climate change.

Data

Calgary, Alberta, serves as the focus of this study due to its rapid urban growth, varied land cover, and strong policy interest in urban heat resilience. With a population of over 1.6 million people, Calgary is the largest city in Alberta and the fourth largest in Canada. Known for its vibrant economy, high-quality public services, and rich cultural offerings, Calgary has ranked among the world's top 10 most livable cities for 11 consecutive years, according to the Economist Intelligence Unit. However, the city also faces challenges associated with the UHI effect, which is intensified by its continental climate, marked by warm summers and cold winters. Urban areas in Calgary often experience higher temperatures than surrounding rural regions, especially during summer heat events. This disparity is not uniformly distributed across the city. Factors such as land use, urban morphology, and access to green spaces contribute to spatial variations in heat exposure, leaving some neighborhoods more vulnerable to the adverse effects of extreme heat. These dynamics underscore the need for targeted strategies to address intra-urban heat risks.

In this study, we use sensor-derived Air temperature (Ta) measurements, collected using 21 ground-based sensors positioned in the central part of Calgary. These sensors were installed to capture a representative range of urban features influencing UHI, such as tree canopy density, built-up area ratios, and water bodies, ensuring comprehensive spatial and environmental coverage. They provide minute-scale temperature readings

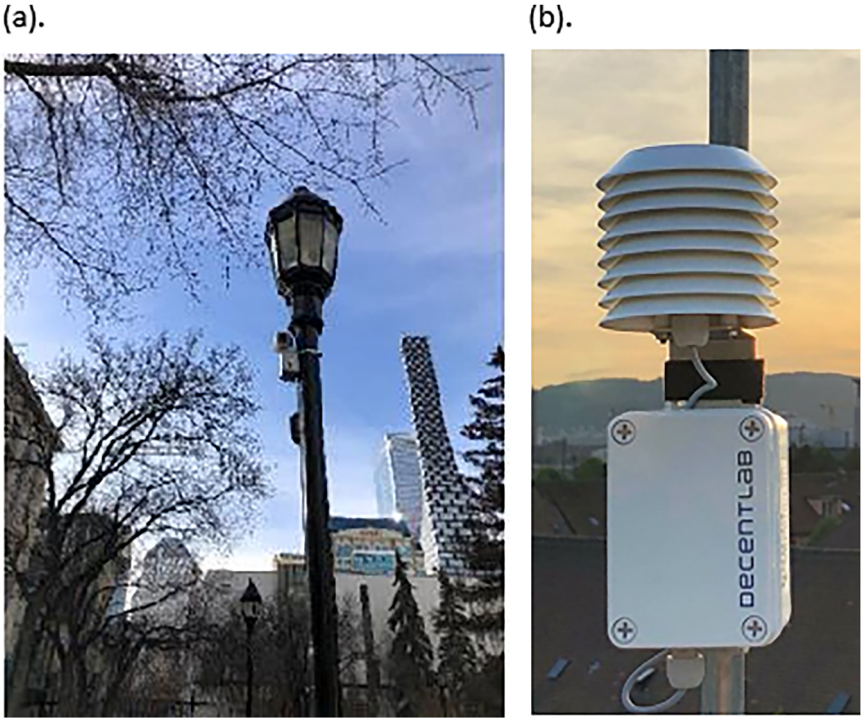

Fig. 7 | Sensor deployment for urban air temperature monitoring in Calgary. Ground-based sensors used to measure ambient air temperature (*T*a) across urban environments: **a** temperature sensor mounted on a lamppost at Olympic Plaza, positioned to capture urban heat variations while minimizing solar radiation biases. **b** A Decent Lab SHT35 ambient temperature sensor with a radiation shield, used across multiple locations in the study to ensure high-precision minute-scale temperature readings. Photographs were provided by the City of Calgary and prepared and formatted by the first author.

from 2021 to 2024, with temporal coverage varying across stations due to different installation dates. The sensor network was specifically designed to ensure high measurement accuracy, with each device calibrated before deployment to maintain data consistency. Additionally, the sensors provide a continuous and detailed record of urban temperature variations, capturing short-term fluctuations. Rigorous quality control measures were applied to ensure data accuracy and consistency. To minimize biases from direct solar exposure, sensors were placed in shaded locations where possible and equipped with radiation shields to reduce the impact of direct and reflected solar radiation on temperature readings. These careful design considerations help mitigate biases, ensuring that the collected data accurately represents ambient air temperature across different urban settings. To ensure accurate alignment between surface and air temperature data, we extracted the exact acquisition time of each Landsat scene from its metadata and matched each surface temperature (*T*s) value with the closest ground-based air temperature (*T*a) reading within a ±15-min window. All feature extraction and preprocessing were carried out in R using sf[95], terra[96], and dplyr[97], while model training and interpretation were implemented in Python using xgboost[98], scikit-learn[99], and shap[100]. Observations with missing or unmatched *T*a values were excluded to maintain temporal consistency and data quality.

Figure 7 exemplifies the location and type of sensors used in this study, showing an installed ambient temperature sensor at Olympic Plaza (panel a) and a Decent Lab SHT35 sensor with a radiation shield (panel b), which ensures accurate air temperature measurements by limiting solar heating effects.

To complement the ground-based air temperature data, Landsat 8 and 9 satellite-derived surface temperature (*T*s) data, accessed through Google Earth Engine, were utilized. These Ts values were derived directly from Landsat imagery captured around 12:30 PM local time (±15 min), corresponding to the satellite overpass time in Calgary. LST was computed using the single-channel method described by Jiménez-Muñoz et al.[101], based on Band 10 thermal data and Planck's equation with a fixed emissivity. This method is commonly used in urban environments where atmospheric correction inputs are limited, providing robust estimates of surface skin temperature at 100 m native resolution, corresponding to the spatial resolution of the Landsat thermal band. In this study, we used the version of LST data that had already been resampled to 30 m within Google Earth Engine, allowing for consistency with other spatial layers and improved integration with 30 m land surface predictors. This approach enabled finer-scale representation of urban temperature patterns across Calgary. The temporal coverage of the satellite data matches that of the air temperature sensors, spanning from 2021 to 2024. A total of 166 Landsat 8 and 9 scenes were acquired between 2021 and 2024. To ensure high-quality observations, we excluded pixels with more than 30% cloud cover using the cloud mask. The exact acquisition time for each Landsat scene was extracted from the satellite metadata to ensure precise temporal alignment. Because Landsat captures imagery around 12:30 PM local time, the resulting dataset reflects only daytime conditions. To balance between the number of data points and the relationship between air temperature (*T*a) and surface temperature (*T*s) on warm days, a threshold of 15°C was selected. This threshold ensures that the data accurately reflects urban heat dynamics during clear, warm conditions, providing a better alignment between *T*a and *T*s during relevant periods. Accordingly, the V-TG model was trained using only the subset of observations where *T*a exceeded 15 °C, ensuring strong performance under elevated temperature conditions most relevant to urban heat analysis.

In addition, the scenario-based hotspot and mitigation analysis was conducted for a single day during the July 2023 heatwave, when much of the city exceeded the 29 °C threshold used by ECCC[61] to define extreme heat events in Calgary. Given the study's goal of modeling air temperature (*T*a) across the city, obtaining Landsat-derived surface temperature (*T*s) is essential for running the model and improving the spatial representation of UHI effects.

The tree canopy ratio (TC) was derived using Remote Sensing software, utilizing the City of Calgary's orthophotography and LiDAR datasets, which are freely available from the City of Calgary Open Data Portal. These datasets were processed using photogrammetric tools to accurately measure tree canopy coverage. Unlike the commonly used normalized difference vegetation index (NDVI), which provides a generalized measure of green space, calculating the tree canopy ratio directly enables a more precise assessment of the tree canopy's impact on UHI effects. This approach offers a significant advantage by focusing specifically on tree canopy coverage,

which plays a critical role in shading and cooling urban environments, thereby providing a clearer understanding of its contribution to mitigating UHI dynamics.

BD is calculated by summing the base areas of all buildings ($A_i; i \in \{1, \ldots, n\}$) in the study area and dividing by the total area (A) of the study unit ($\mathrm{BD} = \sum_{i=1}^{n} \frac{A_i}{A}$). This metric quantifies the concentration of buildings, which affects heat retention due to reduced airflow and increased impervious surfaces[102–105]. The 3D building shapes are derived from full-surface LiDAR data, with roof surface outlines provided openly by the City of Calgary open data.

BH is calculated as the average height of all buildings ($H_i; i \in \{1, \ldots, n\}$) in the study area ($\mathrm{BH} = \sum_{i=1}^{n} \frac{H_i}{n}$). This factor reflects the vertical structure of urban environments, with taller buildings contributing to shading effects and influencing local temperature gradients[86,103–105]. The BH data are based on 3D building shapes derived from full-surface LiDAR data.

The FAR is computed by summing the base areas of each building (A_i) multiplied by the number of floors (H_i) and dividing by the total area (A) of the study area $\mathrm{FAR} = \sum_{i=1}^{n} \frac{A_i H_i}{A}$. FAR indicates the level of urbanization and contributes to heat retention in built-up areas[102–106].

The SVF is calculated by averaging the vertical elevation angles (γ_i) from a set of directions n, where a lower SVF indicates greater enclosure of the urban area and thus more solar radiation absorption ($\mathrm{SVF} = 1 - \frac{\sum_{i=1}^{n} \sin \gamma_i}{n}$)[69,86,107–109]. We used the shadow package in R to calculate this factor[110].

SH represents the vertical extent of shadows cast by buildings in the study area, calculated using the *shadow* package[110] in R. It is determined by the height of buildings and their spatial orientation relative to the sun's position at specific times of day. Higher SHs reduce solar exposure on adjacent surfaces, thereby influencing localized temperature gradients and potentially mitigating UHI effects. This variable captures the interplay between urban geometry and solar radiation, which affects both thermal comfort and energy balance in urban environments. Studies have highlighted its significant role in shaping microclimatic conditions and influencing surface temperatures.

The ratios of impervious surfaces, such as concrete (SR-C), pavement (SR-P), and gravel (SR-G) or mixed (SR-M), to pervious surfaces like water (SR-W) were derived from the City of Calgary's open datasets, specifically from Calgary Digital Aerial Survey mapping linework, which identifies areas classified as impervious. These datasets provide a detailed view of the city's surface composition. The impervious surfaces are typically associated with increased surface temperatures, contributing to the UHI effect by retaining heat. In contrast, pervious surfaces such as water and vegetation help reduce heat retention, offering cooling benefits to urban environments.

Climate data, including WS, WD, and relative humidity (H), were derived from the same sensor network used for collecting air temperature (Ta) data across Calgary, with a minute temporal scale. These factors influence both Ta and Ts by modulating heat dispersion and retention in the urban environment. By integrating these features, the V-TG model estimates the temperature anomaly (Ts–Ta) at different spatial scales (i.e., buffer radius), providing high-resolution insights into temperature relationships across the city. The integration of climate data with urban morphology and land cover characteristics in the modeling framework is visually represented in Fig. 6, illustrating the combined role of these factors in estimating urban temperature variations.

Data availability

The land surface temperature (LST) data used in this study were derived from Landsat 8 and Landsat 9 thermal infrared imagery and are publicly accessible through the Google Earth Engine platform at https://developers.google.com/earth-engine/datasets/catalog/landsat. Urban morphology variables, including building height, building footprint area, floor area ratio (FAR), and other geometry-related attributes, were estimated based on the City of Calgary Open Data Portal and can be accessed at http://data.calgary.ca/Base-Maps/Buildings/uc4c-6kbd/about_data. Surface type classifications, including impervious and pervious surfaces, were sourced from the same portal and are available at http://data.calgary.ca/Environment/Impervious-Surface-2021/rgsu-3v7u/about_data. The tree canopy dataset, which was derived using high-resolution orthophotos and LiDAR scans provided by the City of Calgary, is publicly available at http://data.calgary.ca/Environment/Tree-Canopy-2022/mn2n-4z98/about_data.

Received: 30 April 2025; Accepted: 25 September 2025;
Published online: 17 November 2025

References

1. Grimm, N. B. et al. Global change and the ecology of cities. *Science* **319**, 756–760 (2008).
2. Kalnay, E. & Cai, M. Impact of urbanization and land-use change on climate. *Nature* **423**, 528–531 (2003).
3. United Nations (UN). *2018 Revision of World Urbanization Prospects* (UN, 2018); https://population.un.org/wup/.
4. He, C. et al. Future global urban water scarcity and potential solutions. *Nat. Commun.* **12**, 4667 (2021).
5. Gui, X., Wang, L., Yao, R., Yu, D. & Li, C. Investigating the urbanization process and its impact on vegetation change and urban heat island in Wuhan, China. *Environ. Sci. Pollut. Res.* **26**, 30808–30825 (2019).
6. Zou, Z. et al. Impacts of land use/ land cover types on interactions between urban heat island effects and heat waves. *Build. Environ.* **204**, 108138 (2021).
7. Chen, G. et al. Global projections of future urban land expansion under shared socioeconomic pathways. *Nat. Commun.* **11**, 537 (2020).
8. Zhao, L. et al. Interactions between urban heat islands and heat waves. *Environ. Res. Lett.* **13**, 034003 (2018).
9. Chen, K., Boomsma, J. & Holmes, H. A. A multiscale analysis of heatwaves and urban heat islands in the western U.S. during the summer of 2021. *Sci. Rep.* **13**, 9570 (2023).
10. Manoli, G. et al. Magnitude of urban heat islands largely explained by climate and population. *Nature* **573**, 55–60 (2019).
11. Gao, S. et al. Urbanization-induced warming amplifies population exposure to compound heatwaves but narrows exposure inequality between global North and South cities. *npj Clim. Atmos. Sci.* **7**, 1–10 (2024).
12. Ramarao, M. V. S. et al. Projected changes in heatwaves over Central and South America using high-resolution regional climate simulations. *Sci. Rep.* **14**, 23145 (2024).
13. Huang, W. T. K. et al. Economic valuation of temperature-related mortality attributed to urban heat islands in European cities. *Nat. Commun.* **14**, 7438 (2023).
14. Tong, S., Prior, J., McGregor, G., Shi, X. & Kinney, P. Urban heat: an increasing threat to global health. *BMJ* **375**, n2467 (2021).
15. Iungman, T. et al. Cooling cities through urban green infrastructure: a health impact assessment of European cities. *Lancet* **401**, 577–589 (2023).
16. Kephart, J. L. & Okoye, S. M. Tackling heat-related mortality in aging populations. *Nat. Med.* **30**, 1247–1248 (2024).
17. Wang, C., Wang, Z.-H., Wang, C. & Myint, S. W. Environmental cooling provided by urban trees under extreme heat and cold waves in U.S. cities. *Remote Sens. Environ.* **227**, 28–43 (2019).
18. Wang, C., Wang, Z.-H. & Yang, J. Cooling effect of urban trees on the built environment of contiguous United States. *Earth's. Future* **6**, 1066–1081 (2018).
19. Eskeland, G. S. & Mideksa, T. K. Electricity demand in a changing climate. *Mitig. Adapt Strateg Glob. Change* **15**, 877–897 (2010).
20. Sivak, M. Potential energy demand for cooling in the 50 largest metropolitan areas of the world: Implications for developing countries. *Energy Policy* **37**, 1382–1384 (2009).

21. Bird, D. N. et al. Estimating the daily peak and annual total electricity demand for cooling in Vienna, Austria by 2050. *Urban Clim.* **28**, 100452 (2019).
22. Gunawardena, K. & Steemers, K. Adaptive comfort assessments in urban neighbourhoods: simulations of a residential case study from London. *Energy Build.* **202**, 109322 (2019).
23. Environment and Climate Change Canada. *Canadian Environmental Sustainability Indicators: Temperature change in Canada* (Environment and Climate Change Canada, 2024); https://www.canada.ca/en/environment-climate-change/services/environmental-indicators/temperature-change.html.
24. Konarska, J., Holmer, B., Lindberg, F. & Thorsson, S. Influence of vegetation and building geometry on the spatial variations of air temperature and cooling rates in a high-latitude city. *Int. J. Climatol.* **36**, 2379–2395 (2016).
25. Bowler, D. E., Buyung-Ali, L., Knight, T. M. & Pullin, A. S. Urban greening to cool towns and cities: a systematic review of the empirical evidence. *Landsc. Urban Plan.* **97**, 147–155 (2010).
26. Ziter, C. D., Pedersen, E. J., Kucharik, C. J. & Turner, M. G. Scale-dependent interactions between tree canopy cover and impervious surfaces reduce daytime urban heat during summer. *Proc. Natl. Acad. Sci. USA* **116**, 7575–7580 (2019).
27. Targino, A. C., Coraiola, G. C. & Krecl, P. Green or blue spaces? Assessment of the effectiveness and costs to mitigate the urban heat island in a Latin American city. *Theor. Appl. Climatol.* **136**, 971–984 (2019).
28. Ramamurthy, P. & Bou-Zeid, E. Heatwaves and urban heat islands: a comparative analysis of multiple cities. *J. Geophys. Res. Atmos.* **122**, 168–178 (2017).
29. Gunawardena, K. & Steemers, K. Assessing the influence of neighbourhood-scale vertical greening application. *Build. Cities* 4, 1. https://doi.org/10.5334/bc.282 (2023).
30. Li, Y. et al. Green spaces provide substantial but unequal urban cooling globally. *Nat. Commun.* **15**, 7108 (2024).
31. Wu, C. et al. Understanding the relationship between urban blue infrastructure and land surface temperature. *Sci. Total Environ.* **694**, 133742 (2019).
32. Chen, S. et al. A high-resolution monitoring approach of canopy urban heat island using a random forest model and multi-platform observations. *Atmos. Meas. Tech.* **15**, 735–756 (2022).
33. McCarthy, H. R. & Pataki, D. E. Drivers of variability in water use of native and non-native urban trees in the greater Los Angeles area. *Urban Ecosyst.* **13**, 393–414 (2010).
34. Schwaab, J. et al. The role of urban trees in reducing land surface temperatures in European cities. *Nat. Commun.* **12**, 6763 (2021).
35. Winbourne, J. B. et al. Tree transpiration and urban temperatures: current understanding, implications, and future research directions. *BioScience* **70**, 576–588 (2020).
36. Haeri, T., Hassan, N. & Ghaffarianhoseini, A. Evaluation of microclimate mitigation strategies in a heterogenous street canyon in Kuala Lumpur from outdoor thermal comfort perspective using Envi-met. *Urban Clim.* **52**, 101719 (2023).
37. Zhang, M. et al. Assessing the impact of fractional vegetation cover on urban thermal environment: a case study of Hangzhou, China. *Sustain. Cities Soc.* **96**, 104663 (2023).
38. Aram, F., García, E. H., Solgi, E. & Mansournia, S. Urban green space cooling effect in cities. *Heliyon* **5**, e01339 (2019).
39. Zhou, W., Wu, T. & Tao, X. Exploring the spatial and seasonal heterogeneity of cooling effect of an urban river on a landscape scale. *Sci. Rep.* **14**, 8327 (2024).
40. Guo, F. et al. Study on the mechanism of urban morphology on river cooling effect in severe cold regions. *Front. Public Health* **11**, 1170627 (2023).
41. Probst, N., Bach, P. M., Cook, L. M., Maurer, M. & Leitão, J. P. Blue green systems for urban heat mitigation: mechanisms, effectiveness and research directions. *Blue-Green. Syst.* **4**, 348–376 (2022).
42. Gunawardena, K. R., Wells, M. J. & Kershaw, T. Utilising green and bluespace to mitigate urban heat island intensity. *Sci. Total Environ.* **584–585**, 1040–1055 (2017).
43. Lin, Y. et al. Water as an urban heat sink: Blue infrastructure alleviates urban heat island effect in mega-city agglomeration. *J. Clean. Prod.* **262**, 121411 (2020).
44. Quan, S. et al. Nonlinear effects of blue-green space variables on urban cold islands in Zhengzhou analyzed with random forest regression. *Front. Ecol. Evol*. **11**, 1185249 (2023).
45. Zhou, Y., Gao, W., Yang, C. & Shen, Y. Exploratory analysis of the influence of landscape patterns on lake cooling effect in Wuhan, China. *Urban Clim.* **39**, 100969 (2021).
46. Manteghi, G., Limit, H. & Remaz, D. Water bodies an urban microclimate: a review. *Mod. Appl. Sci.* **9**, p1 (2015).
47. Yao, L., Sailor, D. J., Yang, X., Xu, G. & Zhao, L. Are water bodies effective for urban heat mitigation? Evidence from field studies of urban lakes in two humid subtropical cities. *Build. Environ.* **245**, 110860 (2023).
48. Li, D. et al. Urban heat island: Aerodynamics or imperviousness?. *Sci. Adv.* **5**, eaau4299 (2019).
49. Chinchilla, J., Carbonnel, A. & Galleguillos, M. Effect of urban tree diversity and condition on surface temperature at the city block scale. *Urban Forest. Urban Green.* **60**, 127069 (2021).
50. Guo, A. et al. Influences of urban spatial form on urban heat island effects at the community level in China. *Sustain. Cities Soc.* **53**, 101972 (2020).
51. Guo, A. et al. Impact of urban morphology and landscape characteristics on spatiotemporal heterogeneity of land surface temperature. *Sustain. Cities Soc.* **63**, 102443 (2020).
52. Venter, Z. S., Chakraborty, T. & Lee, X. Crowdsourced air temperatures contrast satellite measures of the urban heat island and its mechanisms. *Sci. Adv.* **7**, eabb9569 (2021).
53. Du, M. et al. Daytime cooling efficiencies of urban trees derived from land surface temperature are much higher than those for air temperature. *Environ. Res. Lett.* **19**, 044037 (2024).
54. Novick, K. A. & Katul, G. G. The duality of reforestation impacts on surface and air temperature. *J. Geophys. Res. Biogeosci.* **125**, e2019JG005543 (2020).
55. Chapman, L., Bell, C. & Bell, S. Can the crowdsourcing data paradigm take atmospheric science to a new level? A case study of the urban heat island of London quantified using Netatmo weather stations. *Int. J. Climatol.* **37**, 3597–3605 (2017).
56. Meier, F., Fenner, D., Grassmann, T., Otto, M. & Scherer, D. Crowdsourcing air temperature from citizen weather stations for urban climate research. *Urban Clim.* **19**, 170–191 (2017).
57. Zumwald, M., Knüsel, B., Bresch, D. N. & Knutti, R. Mapping urban temperature using crowd-sensing data and machine learning. *Urban Clim.* **35**, 100739 (2021).
58. Cao, J., Zhou, W., Zheng, Z., Ren, T. & Wang, W. Within-city spatial and temporal heterogeneity of air temperature and its relationship with land surface temperature. *Landsc. Urban Plan.* **206**, 103979 (2021).
59. Mohajerani, A., Bakaric, J. & Jeffrey-Bailey, T. The urban heat island effect, its causes, and mitigation, with reference to the thermal properties of asphalt concrete. *J. Environ. Manag.* **197**, 522–538 (2017).
60. Grimmond, C. S. B. Progress in measuring and observing the urban atmosphere. *Theor. Appl. Climatol.* **84**, 3–22 (2006).
61. ECCC, E. and C. C. *Extreme Heat Events* (Government of Canada, 2025); https://www.canada.ca/en/environment-climate-change/services/environmental-indicators/extreme-heat-events.html.
62. Overeem, A. et al. Crowdsourcing urban air temperatures from smartphone battery temperatures. *Geophys. Res. Lett.* **40**, 4081–4085 (2013).

63. Doda, T. et al. Lake surface cooling drives littoral-pelagic exchange of dissolved gases. *Sci. Adv.* **10**, eadi0617 (2024).
64. Haddad, S. et al. Holistic approach to assess co-benefits of local climate mitigation in a hot humid region of Australia. *Sci. Rep.* **10**, 14216 (2020).
65. Cheng, X., Peng, J., Dong, J., Liu, Y. & Wang, Y. Non-linear effects of meteorological variables on cooling efficiency of African urban trees. *Environ. Int.* **169**, 107489 (2022).
66. Wang, J. et al. Assessing summer thermal environment in humid cities: local climate zone perspective. *iScience* **28**, 112758 (2025).
67. Feng, X., Wen, H., He, M. & Xiao, Y. Microclimate effects and influential mechanisms of four urban tree species underneath the canopy in hot and humid areas. *Front. Environ. Sci*. **11**, 1108002 (2023).
68. Li, Z.-L. et al. Satellite remote sensing of global land surface temperature: definition, methods, products, and applications. *Rev. Geophys.* **61**, e2022RG000777 (2023).
69. Dirksen, M., Ronda, R. J., Theeuwes, N. E. & Pagani, G. A. Sky view factor calculations and its application in urban heat island studies. *Urban Clim.* **30**, 100498 (2019).
70. Siu, L. W. & Hart, M. A. Quantifying urban heat island intensity in Hong Kong SAR, China. *Environ. Monit. Assess.* **185**, 4383–4398 (2013).
71. Yuan, C. & Chen, L. Mitigating urban heat island effects in high-density cities based on sky view factor and urban morphological understanding: a study of Hong Kong. *Architect. Sci. Rev.* **54**, 305–315 (2011).
72. Jiao, M., Jenerette, G. D., Zhou, W., Wang, J. & Zheng, Z. Adaptive shading: How microclimates and surface types amplify tree cooling effects?. *Urban Forest. Urban Green.* **101**, 128546 (2024).
73. Oke, T. R., Mills, G., Christen, A. & Voogt, J. A. *Urban Climates* (Cambridge University Press, Cambridge, 2017); https://doi.org/10.1017/9781139016476.
74. Coutts, A. M., White, E. C., Tapper, N. J., Beringer, J. & Livesley, S. J. Temperature and human thermal comfort effects of street trees across three contrasting street canyon environments. *Theor. Appl. Climatol.* **124**, 55–68 (2016).
75. Li, Y., Schubert, S., Kropp, J. P. & Rybski, D. On the influence of density and morphology on the Urban Heat Island intensity. *Nat. Commun.* **11**, 2647 (2020).
76. Joshi, K., Khan, A., Anand, P. & Sen, J. Understanding the synergy between heat waves and the built environment: a three-decade systematic review informing policies for mitigating urban heat island in cities. *Sustain. Earth Rev.* **7**, 25 (2024).
77. Du, H. et al. Simultaneous investigation of surface and canopy urban heat islands over global cities. *ISPRS J. Photogramm. Remote Sens.* **181**, 67–83 (2021).
78. Lai, J., et al. Reconciling debates on the controls on surface urban heat island intensity: effects of scale and sampling. *Geophys. Res. Lett.* **48**, e2021GL094485 (2021).
79. Du, H. et al. Exacerbated heat stress induced by urban browning in the Global South. *Nat Cities* https://doi.org/10.1038/s44284-024-00184-9 (2025).
80. Benz, S. A. & Burney, J. A. Widespread race and class disparities in surface urban heat extremes across the United States. *Earth's. Future* **9**, e2021EF002016 (2021).
81. Chakraborty, T., Hsu, A., Manya, D. & Sheriff, G. Disproportionately higher exposure to urban heat in lower-income neighborhoods: a multi-city perspective. *Environ. Res. Lett.* **14**, 105003 (2019).
82. Stott, I., Soga, M., Inger, R. & Gaston, K. J. Land sparing is crucial for urban ecosystem services. *Front. Ecol. Environ.* **13**, 387–393 (2015).
83. Geschke, A., James, S., Bennett, A. F. & Nimmo, D. G. Compact cities or sprawling suburbs? Optimising the distribution of people in cities to maximise species diversity. *J. Appl. Ecol.* **55**, 2320–2331 (2018).
84. Cai, Z., Demuzere, M., Tang, Y. & Wan, Y. The characteristic and transformation of 3D urban morphology in three Chinese mega-cities. *Cities* **131**, 103988 (2022).
85. Elith, J., Leathwick, J. R. & Hastie, T. A working guide to boosted regression trees. *J. Anim. Ecol.* **77**, 802–813 (2008).
86. Guo, A. et al. Divergent impact of urban 2D/3D morphology on thermal environment along urban gradients. *Urban Clim.* **45**, 101278 (2022).
87. Zhang, Y. & Haghani, A. A gradient boosting method to improve travel time prediction. *Transport. Res. Part C Emerg. Technol.* **58**, 308–324 (2015).
88. Friedman, J. H. Greedy function approximation: a gradient boosting machine. *Ann. Stat.* **29**, 1189–1232 (2001).
89. Chen, T. & Guestrin, C. XGBoost: a scalable tree boosting system. In *Proc the 22nd ACM SIGKDD International Conference on Knowledge Discovery and Data Mining* 785–794 (Association for Computing Machinery, New York, 2016); https://doi.org/10.1145/2939672.2939785.
90. Soltani, A. & Lee, C. L. The non-linear dynamics of South Australian regional housing markets: a machine learning approach. *Appl. Geogr.* **166**, 103248 (2024).
91. Tanoori, G., Soltani, A. & Modiri, A. Machine learning for urban heat island (UHI) analysis: predicting land surface temperature (LST) in urban environments. *Urban Clim.* **55**, 101962 (2024).
92. Bergstra, J. & Bengio, Y. Random search for hyper-parameter optimization. *J. Mach. Learn. Res.* **13**, 281–305 (2012).
93. Shapley, L. S. Stochastic games*. *Proc. Natl. Acad. Sci. USA* **39**, 1095–1100 (1953).
94. Lundberg, S. M. & Lee, S.-I. A unified approach to interpreting model predictions. In *Advances in Neural Information Processing Systems* (Curran Associates, Inc., 2017).
95. Pebesma, E. et al. *sf: Simple Features for R* (RSS, 2025).
96. Hijmans, R. J. et al. *terra: Spatial Data Analysis* (rspatial, 2025).
97. Wickham, H. et al. *dplyr: A Grammar of Data Manipulation* (dplyr, 2023).
98. Cho, H. *XGBoost Python Package—xgboost 3.0.2 documentation* (XGBoost, 2025); https://xgboost.readthedocs.io/en/stable/python/.
99. Pedregosa, F. et al. Scikit-learn: machine learning in python. *J. Mach. Learn. Res.* **12**, 2825–2830 (2011).
100. Lundberg, S. M. *A Unified Approach to Explain the Output of Any Machine Learning Model*, (NIPS, 2025).
101. Jiménez-Muñoz, J. C., Sobrino, J. A., Skoković, D., Mattar, C. & Cristóbal, J. Land surface temperature retrieval methods from Landsat-8 thermal infrared sensor data. *IEEE Geosci. Remote Sens. Lett.* **11**, 1840–1843 (2014).
102. Azhdari, A., Soltani, A. & Alidadi, M. Urban morphology and landscape structure effect on land surface temperature: evidence from Shiraz, a semi-arid city. *Sustain. Cities Soc.* **41**, 853–864 (2018).
103. Cai, Z., Han, G. & Chen, M. Do water bodies play an important role in the relationship between urban form and land surface temperature?. *Sustain. Cities Soc.* **39**, 487–498 (2018).
104. Chen, Y. et al. Relationship between urban spatial form and seasonal land surface temperature under different grid scales. *Sustain. Cities Soc.* **89**, 104374 (2023).
105. Zhang, Z. et al. The influences of 2D/3D urban morphology on land surface temperature at the block scale in Chinese megacities. *Urban Clim.* **49**, 101553 (2023).
106. Yin, C., Yuan, M., Lu, Y., Huang, Y. & Liu, Y. Effects of urban form on the urban heat island effect based on spatial regression model. *Sci. Total Environ.* **634**, 696–704 (2018).
107. Guo, J., Han, G., Xie, Y., Cai, Z. & Zhao, Y. Exploring the relationships between urban spatial form factors and land surface temperature in mountainous area: a case study in Chongqing city, China. *Sustain. Cities Soc.* **61**, 102286 (2020).
108. Ramírez-Aguilar, E. A. & Lucas Souza, L. C. Urban form and population density: influences on urban heat island intensities in Bogotá, Colombia. *Urban Clim.* **29**, 100497 (2019).

109. Zhang, N., Zhang, J., Chen, W. & Su, J. Block-based variations in the impact of characteristics of urban functional zones on the urban heat island effect: a case study of Beijing. *Sustain. Cities Soc.* **76**, 103529 (2022).
110. Dorman, M., Erell, E., Vulkan, A. & Kloog, I. shadow: R package for geometric shadow calculations in an urban environment. *R. J.* **11**, 287–309 (2019).

Acknowledgements

We gratefully acknowledge Mitacs and the City of Calgary for providing funding and technical support for this project, and in particular thank Florentin Wecxsteen, Jillian Prosser, and Stacey Rector for their support. We also thank the City of Calgary for providing access to sensor data used in this study. We appreciate the constructive feedback provided by the two anonymous reviewers and the editorial guidance of Dr. Anjal Prakash, which helped improve the quality of this manuscript.

Author contributions

M.Z., S.M.P., and A.P. led the conceptualization and methodology. M.Z. conducted the investigation, visualization, and wrote the original draft. S.M.P. and A.P. contributed to the investigation and review, and editing of the manuscript.

Competing interests

The authors declare no competing interests.

Additional information

Supplementary information The online version contains supplementary material available at https://doi.org/10.1038/s42949-025-00277-x.

Correspondence and requests for materials should be addressed to Masoud Zaerpour.